

# Distribution rules of systematic absence and generalized de Wolff figure of merit applied to EBSD ab-initio indexing

R. Oishi-Tomiyasu<sup>a,b</sup>, T. Tanaka<sup>c</sup>, and J. Nakagawa<sup>c</sup>

<sup>a</sup>Yamagata University, Yamagata, Japan\*

<sup>b</sup>JST PRESTO, Kawaguchi, Japan

<sup>c</sup>Nippon Steel Corporation, Japan

November 17, 2020

## Abstract

For EBSD ab-initio indexing, a new method that adopts several methods originally invented for powder indexing, is reported. Distribution rules of systematic absence and error-stable Bravais lattice determination are used to eliminate negative influence of non-visible bands and erroneous information from visible bands. In addition, generalized versions of the de Wolff figures of merit are proposed as a new sorting criterion for the obtained unit-cell parameters, which can be used in both orientation determination and ab-initio indexing from Kikuchi patterns. Computational results show that the new figures of merit work well, similarly to the original de Wolff  $M_n$ . Ambiguity of indexing solutions is also pointed out, which happens in particular for low-symmetric cells, and may generate multiple distinct solutions even if very accurate positions of band center lines and the projection center are given.

## 1 Introduction

Electron backscatter diffraction (EBSD) is a characterization technique for the microstructure of crystalline or polycrystalline materials, developed by Venable & Harland (1973), and later refined by Dingley & Baba-Kishi (1986) with an aid of computers. This technique can be applied for the determination of crystal orientation, texture analysis, phase identification and strain analysis (Troost *et al.* (1993); Wilkinson *et al.* (2006); Tanaka *et al.* (2019)).

In orientation determination, the unit-cell parameters are priorly given. The center lines of the Kikuchi bands are utilized for acquisition of the unit-cell orientation (Wright & Adams, 1992; Kogure, 2003). However, in EBSD ab-initio indexing, the unit-cell parameters and its symmetry are also determined. For any fixed  $hkl$ , all the bands with the indices  $m(hkl)$  ( $m$ : integer) completely overlap in EBSD patterns. Hence, all the derivative lattices (*e.g.*, sublattices and superlattices) of the true solution have identical positions of Kikuchi center lines. As a result, reliable information about  $d$ -spacings contained *e.g.*, in the widths of Kikuchi bands is indispensable for uniquely determining the solution.

The band width is approximately proportional to the inverse of the interplanar spacing (*i.e.*,  $d$ -spacings) of the diffracting plane. This information has been used for EBSD ab-initio indexing (Michael (2000); Dingley & Wright (2009); Li & Han (2015)), including the recent software EBSDL [Li *et al.*, 2014].

Due to the complex profile of band edges (Nolze *et al.* (2015); Nolze & Winkelmann (2017)), and also due to the small Bragg angle caused by short wavelengths of the incident electron beam, the error in the band-width measurement is 5-20% [Dingley and Wright, 2009]. Better accuracy could be obtained by analyzing the higher-order Laue Zone (HOLZ) rings (Michael & Eades (2000); Langer & Däbritz (2007); Dingley & Wright (2009)). However, it is not straightforward to analyze the  $d$ -spacings from the HOLZ rings [Nolze *et al.*, 2015], and it depends on the crystal structure whether the HOLZ rings are clearly visible.

---

\*E-mail: tomiyasu@imi.kyushu-u.ac.jp, Current affiliation: Institute of Mathematics for Industry (IMI), Kyushu University

Therefore, the  $d$ -spacings extracted from the bandwidths are also used in this article, although our improvements can be similarly applied to the analyses based on HOLZ rings.

Technically, the novel points of our indexing method are as follows:

- (1) Non-visible band edges in EBSD patterns, are frequently caused by reflections with relatively small structure factors [Nolze and Winkelmann, 2017]. We propose a method that works for all the types of systematic absence (SA), as a result of the theorems in Oishi-Tomiyasu (2013) that are available without any prior information on the Bravais types and the space groups.
- (2) our method for error-stable Bravais lattice determination [Oishi-Tomiyasu, 2012], and new figures of merit with a definition similar to the de Wolff figure of merit [de Wolff, 1968], are applied to EBSD indexing for the first time.

As for (1), the method of Dingley & Wright (2009) needs a reciprocal-lattice basis  $l_1^*, l_2^*, l_3^*$  such that all of  $l_1^*, -l_i^*, l_1^* + l_i^*$  are not extinct for both  $i = 2, 3$ , although such a basis does not exist for some space groups and settings (*e.g.*, No.70  $c, d$ , No.88  $c, d$ ). It is explained in Section 2 how to extract information about non-visible bands from visible bands, without being adversely affected by forbidden reflections. However, with regard to SAs, Day (2008) reported that in the experimental pattern of  $Si$ , the bandwidth of the forbidden  $\{222\}$  was the most visible among all of  $\{hhh\}$ . Therefore, reflection rules might be violated to some degree owing to dynamic scattering of the electron beam.

With regard to the Bravais lattice determination, even very small errors in unit-cell parameters such as rounding errors can cause failure in Bravais lattice determination [Grosse-Kunstleve et al., 2004]. Owing to this, the first author provided a method for error-stable Bravais lattice determination with rigorous proofs in Oishi-Tomiyasu (2012), as explained in Section 3.2.

We also propose figures of merit for orientation determination and ab-initio indexing (Section 4), by extending the definition of the de Wolff figure of merit. The de Wolff  $M_n$  has been used as the most efficient indicator in powder indexing (1D data), and the generalized ones are presenting very similar properties to those of the original one.

In this article, an ambiguity of solutions in EBSD ab-initio indexing, which sometimes allows multiple distinct solutions, are also explained. This is different from the ambiguity reported in Alkorta (2013) (explained in Sections 2 and 3.2), and happens when many observed bandwidths are not the narrowest ones. In this case, the above uniqueness problem occurs again, because all the sublattices of the true crystal lattice can have identical bandwidths, in addition to the band positions. Thus, in ab-initio indexing, it is necessary to assume that the edges of the narrowest bands are the most visible at least for several bands. Otherwise, the assumption that the unit cell has higher-symmetric Bravais type can be used to resolve this ambiguity.

Lastly, the developed program and the source codes are available from the web site: <http://ebbsd-conograph.osdn.jp/InstructionsEBSDConograph.html>.

For definition, the 3-dimensional (3D) lattice  $M$  is a *derivative lattice* of another 3D lattice  $L$ , if they have a common 3D sublattice  $M \cap L$ .

## 2 Background and formulas for EBSD indexing

A general method to gain the unit-cell length-ratios and angles from the center-line positions of the Kikuchi bands (in particular without bandwidths) is explained herein. The used notation is basically the same as that in Kogure (2003).

The general situation of electron backscattering is depicted in Figure 1. In Figures 1 and 2, it may be thought that the positions of the projection centers are exact, even if they are unknown. Although the relationship between Kikuchi bands is often explained by using the coordinates of Kikuchi bands, the same thing is more easily understood by using the projected coordinates of the reciprocal lattice points, which are computable from the parameters of the band center lines.

In Figure 1 (a), the three axes  $x_1, x_2, x_3$  orthogonal to each other, are fixed so that the third axis  $x_3$  is perpendicular to the phosphor screen. Since the scale is adjusted so that the camera length equals 1, the pattern center  $O$  on the phosphor screen exists at the coordinate  $(0, 0, 1)$ .

The Kikuchi center lines are the intersections of diffracting planes and the phosphor screen. As in Figure 1 (a), the coordinate of each center lines (more precisely, the foot of the perpendicular from the pattern center  $O$  to the Kikuchi center line) can be represented as  $(x_1, x_2, x_3) = (\tan \sigma \cos \varphi, \tan \sigma \sin \varphi, 1)$ ,

by using its spherical coordinate  $(r, \sigma, \varphi)$  with  $r = 1/\cos$ . The perpendicular direction coincides with the direction of the reciprocal-lattice vectors  $m\mathbf{a}^*$  ( $m \neq 0$ : integer). Namely,

$$\begin{aligned}\mathbf{a}^* &\propto \left( -\frac{\cos \varphi}{\tan \sigma}, -\frac{\sin \varphi}{\tan \sigma}, 1 \right), \\ &\propto (-\cos \sigma \cos \varphi, -\cos \sigma \sin \varphi, \sin \sigma).\end{aligned}$$

As a result, as shown in Figure 1(b), the reciprocal-lattice vector  $\mathbf{a}^*$  that provides the Miller index of the Kikuchi band at  $(x_1, x_2) = (\tan \sigma \cos \varphi, \tan \sigma \sin \varphi)$  is projected to the coordinate  $(x_1, x_2) = (-\cos \varphi / \tan \sigma, -\sin \varphi / \tan \sigma)$  on the screen.

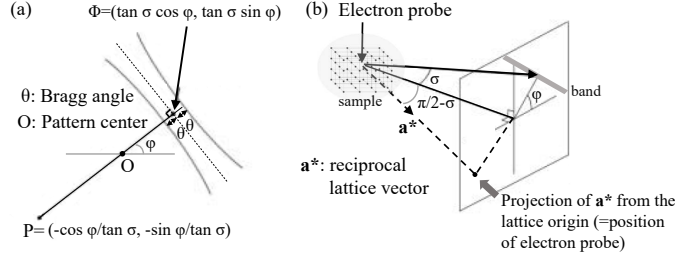


Figure 1: Relationship between the center line of a Kikuchi band and the direction of the corresponding reciprocal lattice vector. In (a), the phosphor screen is parallel to the sheet. In both (a) and (b), the scale is adjusted so that the camera length (= distance from the electron probe to the screen) equals 1.

This interpretation is useful for obtaining a geometric intuition of Kikuchi patterns. In particular, the bands with the Miller indices  $m(hkl)$  (equivalently, reciprocal lattice vectors  $m\mathbf{a}^*$ ,  $m \neq 0$ : integer) have an identical center line. Furthermore, the three projected lattice points  $P_1, P_2, P_3$  are aligned on the phosphor screen, if and only if they correspond to coplanar reciprocal lattice vectors. As is well known, this happens if and only if the corresponding Kikuchi lines intersect at one point (Figure 2).

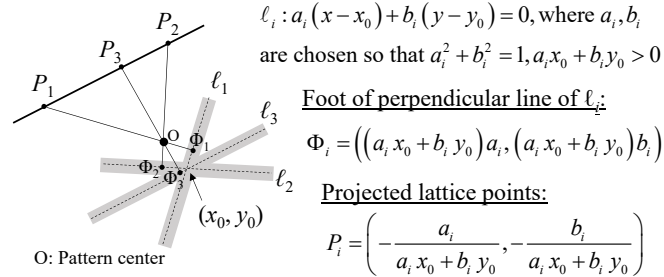


Figure 2: Kikuchi bands intersecting at one point; if all the Kikuchi lines  $\ell_i$  ( $i = 1, 2, 3$ ) intersect at  $(x_0, y_0)$ , their corresponding projected lattice points  $P_i$  are on the line  $x_0 X + y_0 Y = -1$ .

This property can be used when one wants to improve results of automatic band detection. Under the projection-center shift  $(\Delta x, \Delta y, \Delta z)$ , the intersection is varied from  $(x_0, y_0)$  to  $(x_0(1 - \Delta z) + \Delta x, y_0(1 - \Delta z) + \Delta y)$  (see Eq.(5), (6) to obtain this).

The ratios of the lattice-vector lengths can be determined from the positions of the Kikuchi lines, as follows; the parameter  $[a_i : b_i]$ ,  $a_i^2 + b_i^2 = 1$  taken as in Figure 2, represents the slope of a band. In this case, the projection  $P_i$  of the corresponding reciprocal lattice vector  $\mathbf{a}_i^*$  has the coordinate  $P_i = (-a_i/(a_i x_0 + b_i y_0), -b_i/(a_i x_0 + b_i y_0))$ . In the 3D-coordinate system, the coordinate of  $P_i$  is equal to  $(-a_i/(a_i x_0 + b_i y_0), -b_i/(a_i x_0 + b_i y_0), 1)$ . Since  $\mathbf{a}_i^*$  and  $P_i$  have the same direction, for some  $c_i > 0$ ,

$$\mathbf{a}_i^* = c_i(-a_i, -b_i, a_i x_0 + b_i y_0).$$

If  $\mathbf{a}_1^*, \mathbf{a}_2^*, \mathbf{a}_3^*$  are coplanar as in Figure 2, some rational numbers  $p, q$  satisfy  $\mathbf{a}_3^* = p\mathbf{a}_1^* + q\mathbf{a}_2^*$ . Hence,

the ratio  $c_1 : c_2 : c_3$  satisfies:

$$\begin{pmatrix} -a_1 & -a_2 & -a_3 \\ -b_1 & -b_2 & -b_3 \\ a_1x_0 + b_1y_0 & a_2x_0 + b_2y_0 & a_3x_0 + b_3y_0 \end{pmatrix} \begin{pmatrix} pc_1 \\ qc_2 \\ -c_3 \end{pmatrix} = 0. \quad (1)$$

If the values of  $p, q$  are given, the ratio  $c_1 : c_2 : c_3$  can be computed from the inner products  $\alpha_{ij} = (a_i, b_i) \cdot (a_j, b_j)$ , owing to  $a_i^2 + b_i^2 = 1$ :

$$\begin{aligned} c_1 : c_2 : c_3 &= \frac{1}{p} \begin{vmatrix} a_2 & a_3 \\ b_2 & b_3 \end{vmatrix} : \frac{1}{q} \begin{vmatrix} a_3 & a_1 \\ b_3 & b_1 \end{vmatrix} : \begin{vmatrix} a_1 & a_2 \\ b_1 & b_2 \end{vmatrix} \\ &= \frac{\sqrt{1 - \alpha_{23}^2}}{|p|} : \frac{\sqrt{1 - \alpha_{13}^2}}{|q|} : \sqrt{1 - \alpha_{12}^2} \end{aligned}$$

The slope  $[a_i : b_i]$  of a Kikuchi line can be determined independently from the position of the pattern center. This explains why the obtained  $c_1 : c_2 : c_3$  are not affected by the error of the pattern center as well. Only the third entry of  $a_ix_0 + b_iy_0$  is affected by the shift  $(\Delta x, \Delta y)$  of  $(x_0, y_0)$ .

In EBSD indexing, if  $(\Delta x, \Delta y)$  are well refined, even if  $\Delta z$  is imprecise, it is possible to index the band center lines, although the  $z$ -scale of the obtained unit-cell parameters might contain large errors owing to the shift  $\Delta z$ . This ambiguity was also pointed out in Alkorta (2013) in a special setting. Eqs.(5), (6) in Section 3.3, explains how  $\Delta z$  and the  $z$ -scale are correlated, when they are simultaneously determined from an EBSD pattern.

In ab-initio indexing, although  $p$  and  $q$  in Eq.(1) are unknown, the ratio  $c_1 : c_2 : c_3$  can be computed by setting  $(p, q)$  to specific values *e.g.*,  $(1, 1)$ ,  $(2, 1)$ , or  $(1, 2)$  as in Section 3.

The Kikuchi bandwidth  $\beta$  on the screen is related to the Bragg angle  $\theta$ , as follows:

$$\beta = \tan(\sigma + \theta) - \tan(\sigma - \theta), \quad (2)$$

The information about the  $d$ -spacing ( $= 1/|m\mathbf{a}^*|$ ) of  $m\mathbf{a}^*$  and its inverse  $d^*$  can be obtained from this  $\theta$  by using the Bragg equation:

$$d^* = \frac{1}{d} = \frac{2 \sin \theta}{\lambda}, \quad (3)$$

where  $\lambda$  is the wavelength of the electron beam.

In practice, it is difficult to obtain accurate values of the bandwidths from experimental patterns, and to judge whether the obtained value corresponds to the narrowest band, although the same thing happens even if HOLZ rings are used [Michael and Eades, 2000].

The following theorems used in Section 3, state that it is not necessary to assign various sets of reciprocal lattice vectors to a combination of the narrowest bands in order to remove all the adverse effect of SA (*e.g.*,  $(p, q) = (2, 1), (1, 2)$  is sufficient to obtain various 2D sublattices, if a number of band edges are available).

In the statements of the theorems,  $L^*$  is the reciprocal lattice of the crystal lattice  $L$ . For simplicity,  $L$  always means the primitive lattice (*i.e.*, the lattice before centering).  $\{l_1^*, l_2^*\}$  is called a *primitive set*, if it is a subset of some basis  $l_1^*, l_2^*, l_3^*$  of  $L^*$ .

**Theorem 1** (Theorem 2 in Oishi-Tomiyasu (2013)). *Regardless of the type of SA, there are infinitely many primitive sets  $\{l_1^*, l_2^*\}$  of  $L^*$  such that none of  $l_1^*, l_2^*, l_1^* + 2l_2^*, 2l_1^* + l_2^*$  corresponds to an extinct reflection due to the SA. Furthermore, there exist infinitely many 2D sublattices  $L_2^*$  of  $L^*$  such that  $L_2^*$  is expanded by such  $l_1^*, l_2^*$ .*

The reciprocal lattices  $l_1^*, l_2^*, l_1^* + 2l_2^*, 2l_1^* + l_2^*$ , and  $l_1^* + l_2^*$  are coplanar. In the method of CONOGRAPH, their relationship is illustrated as in Figure 3, by using a graph:

**Theorem 2** (Theorem 4 in Oishi-Tomiyasu (2013)). *Regardless of the type of SA, there are infinitely many bases  $\{l_1^*, l_2^*, l_3^*\}$  of  $L^*$  such that the following hold:*

- (a) *the reflections of  $\pm l_1^* + l_2^* + l_3^*$  are not forbidden.*
- (b) *For both  $i = 2, 3$ , (i) none of the reflections of  $ml_1^* + (m-1)(-l_1^* + l_i^*)$  are forbidden for any integer  $m$ , or otherwise, (ii) none of the reflections of  $ml_i^* + (m-1)(l_1^* - l_i^*)$  are forbidden for any integer  $m \geq 0$ .*

That is, none of the underlined lattice vectors in Figure 4 corresponds to a forbidden reflection.

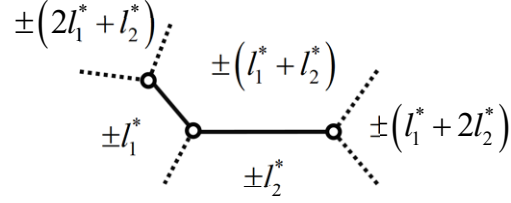


Figure 3: A subgraph of a topograph corresponding to the reflections  $l_1^*$ ,  $l_2^*$ ,  $l_1^* + 2l_2^*$ ,  $2l_1^* + l_2^*$  that are not forbidden, and  $l_1^* + l_2^*$  that might be forbidden owing to SA. This graph was originally used in Conway (1997), where the term “topograph” was first coined.

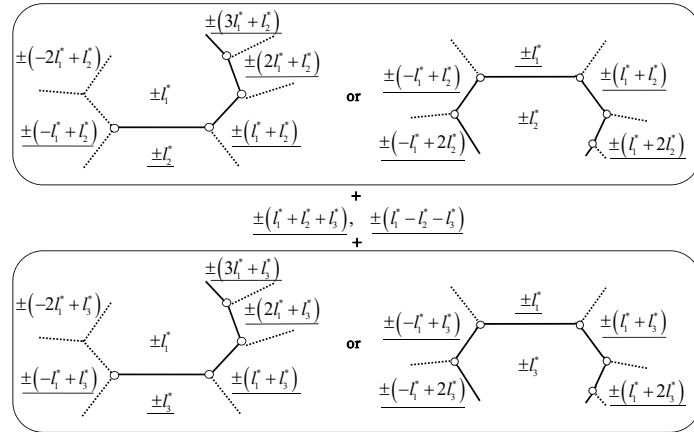


Figure 4: Outline of Theorem 2, which ensures that none of the underlined lattice vectors are forbidden.

### 3 New methods for ab-initio EBSD indexing and scale determination of the unit-cell

#### 3.1 Acquisition of candidates for the primitive lattice

Ab-initio indexing methods can be classified into two categories, depending on their strategy. In the first category, various  $hkl$ s are assigned to a few selected reflections, in order to generate multiple candidate solutions. The advantage of the latter is that the true solution is normally generated multiple times from distinct observed reflections, hence it can be robust against errors in the input.

Our method belongs to the latter. The basic algorithm, which uses only the positions of the Kikuchi center lines, is provided in Table 1.

Unlike step (3-a) in which the direction of  $\mathbf{a}_1^* + \mathbf{a}_2^*$  is observed, in steps (3-b) and (3-c),  $\mathbf{a}_1^* + \mathbf{a}_2^*$  predicted from the other input bands is stored in  $\mathcal{A}$ . The algorithm is simplified by this use of virtual bands. Figure 5 shows which combinations of visible bands and non-visible bands are used to construct a unit cell.

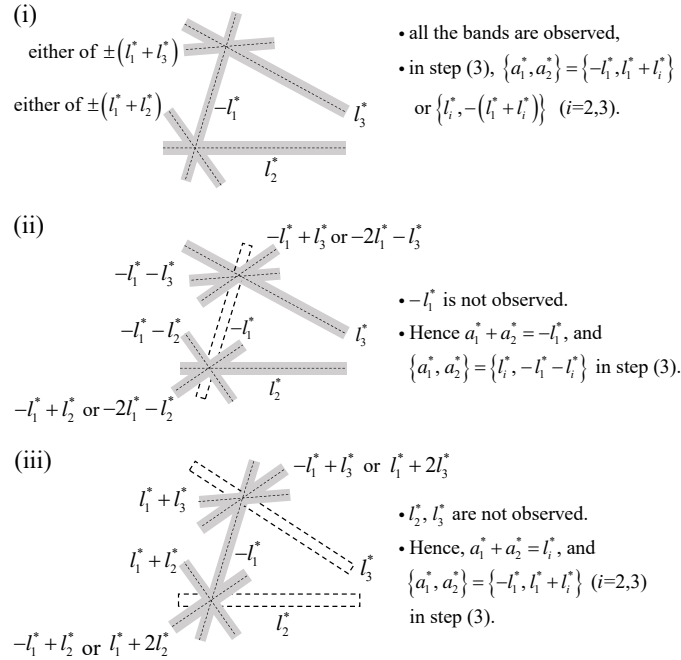


Figure 5: Combinations of bands and their reciprocal lattice vectors assigned for indexing. If 5 or 6 bands intersect as in either of (i)–(iii), the lattice basis  $(\mathbf{b}_1^*, \mathbf{b}_2^*, \mathbf{b}_3^*) = (-l_1^*, l_2^*, l_3^*)$  is saved in step (4) of Table 1. All of their length-ratios and inner products are determined from the band positions. Every observed band (gray) and computed band (white) are assigned either of  $\pm l_1^*$ ,  $\pm l_2^*$ ,  $\pm l_3^*$ , or their linear sums  $\pm(l_1^* \pm l_i^*)$ ,  $\pm(2l_1^* + l_i^*)$ ,  $\pm(l_1^* + 2l_i^*)$  ( $i = 2, 3$ ). These vectors assigned to the observed bands are chosen from the underlined not-forbidden reflections in Figure 4.

So far, although Theorems 1, 2 have been used to determine which sets of vectors should be assigned to bands, it is unnecessary to consider SAs, because of the overlay of the bands of  $m(hkl)$  ( $m$ : integer). SAs (and the breakdown of Friedel's law [Marthinsen and Høier, 1988]) do not largely influence on the band positions. However, information about bandwidths are used in step (3) in order to obtain the lengths of  $\mathbf{a}_i^*$ ,  $\mathbf{a}_1^* + \mathbf{a}_2^*$ . SAs influence in this case, because it is assumed that the edges of the narrowest bands are input for the visible bands.

At runtime, our algorithm normally generates multiple times almost identical lattices from different combinations of observed bands. The unit-cell scales are also computed for each combination.

Table 1: Indexing algorithm in which only the positions of Kikuchi center lines are used.

(Input)

**Inp:** array of unit vectors  $\mathbf{u} = (-\cos \sigma \cos \varphi, -\cos \sigma \sin \varphi, \sin \sigma)$  obtained from the Kikuchi band center positions  $(\tan \sigma \cos \varphi, \tan \sigma \sin \varphi)$  on the screen (the positions may be affected by the error of the projection center).

(Output)

**Ans:** array of candidates for the reciprocal lattice basis (here, the basis vectors are the edges of the primitive cell).

(Algorithm)

**Detection of zones (2D sublattices):**

- (1) for any distinct vectors  $\mathbf{u}_1 \neq \mathbf{u}_2$  in **Inp**, search for all the  $\mathbf{u}_3$  in **Inp** that may be considered to be linearly dependent on  $\mathbf{u}_1, \mathbf{u}_2$ . All of such  $\mathbf{u}_3$  are saved in a new array **Inp<sub>u<sub>1</sub>,u<sub>2</sub></sub>**.
- (2)  $\langle$ Computation of  $\lambda_1, \lambda_2$  with  $\mathbf{u}_3 = \lambda_1 \mathbf{u}_1 + \lambda_2 \mathbf{u}_2$  $\rangle$  for each  $\mathbf{u}_3 \in \mathbf{Inp}_{\mathbf{u}_1, \mathbf{u}_2}$ , the following equation is solved:

$$\begin{pmatrix} u_{11} & u_{21} & u_{31} \\ u_{12} & u_{22} & u_{32} \end{pmatrix} \begin{pmatrix} \lambda_1 \\ \lambda_2 \\ -1 \end{pmatrix} = 0,$$

where  $(u_{i1}, u_{i2}, u_{i3})$  are the entries of  $\mathbf{u}_i$  ( $i = 1, 2, 3$ ). If  $\lambda_1 \leq 0$  or  $\lambda_2 \leq 0$ , go to the next  $\mathbf{u}_3 \in \mathbf{Inp}_{\mathbf{u}_1, \mathbf{u}_2}$ . Otherwise, carry out step (3) and store a pair of vectors  $\{\mathbf{a}_i^*, \mathbf{a}_1^* + \mathbf{a}_2^*\}$  ( $i = 1, 2$ ) in a common array  $\mathcal{A}$ , before going to the next  $\mathbf{u}_3$ .

- (3) In what follows,  $\mathbf{a}_i^*$  is the reciprocal lattice vector with the direction  $\mathbf{u}_i$  ( $i = 1, 2, 3$ ). The assumption  $\mathbf{a}_3^* = p\mathbf{a}_1^* + q\mathbf{a}_2^*$  is tested for each of  $(p, q) = (1, 1), (2, 1), (1, 2)$  in the following (3-a)–(3-c):
- (3-a) (Case of  $(p, q) = (1, 1)$ , *i.e.*,  $\mathbf{a}_3^* = \mathbf{a}_1^* + \mathbf{a}_2^*$ ) in this case,  $|\mathbf{a}_1^*| : |\mathbf{a}_2^*| : |\mathbf{a}_3^*| = \lambda_1 : \lambda_2 : 1$  holds (*cf.* Eq.(1)). Hence,  $\{\lambda_1 \mathbf{u}_1, \mathbf{u}_3\}, \{\lambda_2 \mathbf{u}_2, \mathbf{u}_3\}$ , are stored in  $\mathcal{A}$ .
- (3-b) (Case of  $(p, q) = (2, 1)$ , *i.e.*,  $\mathbf{a}_3^* = 2\mathbf{a}_1^* + \mathbf{a}_2^*$ ) Similarly,  $|\mathbf{a}_1^*| : |\mathbf{a}_2^*| : |\mathbf{a}_3^*| = \lambda_1/2 : \lambda_2 : 1$  is obtained. Hence  $\mathbf{a}_1^*, \mathbf{a}_2^*, \mathbf{a}_1^* + \mathbf{a}_2^*$  are constant multiples of  $(\lambda_1/2)\mathbf{u}_1, \lambda_2 \mathbf{u}_2, (\lambda_1/2)\mathbf{u}_1 + \lambda_2 \mathbf{u}_2$ . If the direction of  $\mathbf{a}_1^* + \mathbf{a}_2^*$  is not observed (*i.e.*, not in **Inp<sub>u<sub>1</sub>,u<sub>2</sub></sub>**),  $\{(\lambda_1/2)\mathbf{u}_1, (\lambda_1/2)\mathbf{u}_1 + \lambda_2 \mathbf{u}_2\}, \{\lambda_2 \mathbf{u}_2, (\lambda_1/2)\mathbf{u}_1 + \lambda_2 \mathbf{u}_2\}$  are stored in  $\mathcal{A}$ .
- (3-c) (Case of  $\langle(p, q) = (1, 2)$ , *i.e.*,  $\mathbf{a}_3^* = \mathbf{a}_1^* + 2\mathbf{a}_2^*$ ) in this case,  $|\mathbf{a}_1^*| : |\mathbf{a}_2^*| : |\mathbf{a}_3^*| = \lambda_1 : \lambda_2/2 : 1$ . Hence  $\mathbf{a}_1^*, \mathbf{a}_2^*, \mathbf{a}_1^* + \mathbf{a}_2^*$  are proportional to  $\lambda_1 \mathbf{u}_1, (\lambda_2/2)\mathbf{u}_2, \lambda_1 \mathbf{u}_1 + (\lambda_2/2)\mathbf{u}_2$ . If the direction of  $\mathbf{a}_1^* + \mathbf{a}_2^*$  is not in **Inp<sub>u<sub>1</sub>,u<sub>2</sub></sub>**,  $\{\lambda_1 \mathbf{u}_1, \lambda_1 \mathbf{u}_1 + (\lambda_2/2)\mathbf{u}_2\}, \{(\lambda_2/2)\mathbf{u}_2, \lambda_1 \mathbf{u}_1 + (\lambda_2/2)\mathbf{u}_2\}$  are stored in  $\mathcal{A}$ .

**Construction of candidates for the lattice basis:**

- (4) for any  $\{\mathbf{b}_1^*, \mathbf{b}_2^*\}, \{\mathbf{cb}_1^*, \mathbf{cb}_3^*\} \in \mathcal{A}$  including vectors  $\mathbf{b}_1^*, \mathbf{cb}_1^*$  with the same direction, if  $\mathbf{b}_1^*, \mathbf{b}_2^*, \mathbf{b}_3^*$  are linearly independent and pass the following check  $(*)^\dagger$ , the basis  $\{\mathbf{b}_1^*, \mathbf{b}_2^*, \mathbf{b}_3^*\}$  is stored in **Ans** as a candidate solution.  
 $(*)^\dagger$  the direction of  $\mathbf{b}_1^* + \mathbf{b}_2^* + \mathbf{b}_3^*$  is observed, *i.e.*, in **Inp**.

<sup>b</sup>The check  $(*)$  is imposed to reduce the number of solutions and computation time. By removing  $(*)$ , it is possible to carry out a more exhaustive search.

### 3.2 Bravais lattice determination & refinement of the projection center, unit-cell parameters and orientation

In Bravais lattice determination, the Bravais-type and the parameters of the conventional cell are determined from the parameters of the primitive cell. The method has been studied by using the lattice-basis reduction theory. For exact unit-cell parameters, the Bravais lattice can be determined by using the 44 lattice characters (Table 9.2.5.1 of International Tables Vol. A [Hahn, 2005]).

Oishi-Tomiyasu (2012) reported a method to extend the Bravais-lattice determination algorithm to general erroneous cases, without increasing calculation time. It is guaranteed to output the correct Bravais type and lattice basis of the conventional cell, except for the case when the input cells contain very huge errors (the precise condition was provided in the cited paper). The program has been used both for determinations under observation errors (*e.g.*, *CONOGRAPH* for powder indexing) and rounding-off errors [Oishi-Tomiyasu, 2016].

This method implemented in the new software, is executed between acquisition of the primitive-cell and the calculation of figures of merit (Figure 6).

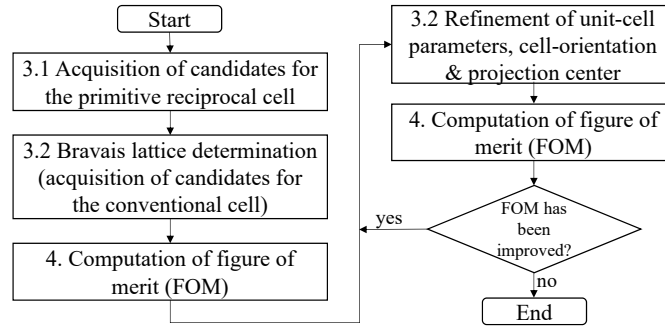


Figure 6: Flowchart of the software; sections 3.1, 3.2, and 4 explain the respective parts.

In the refinement stage, the following parameters are fit to the band positions (and widths, according to the user's choice):

- $s$ : scale of the unit cell.
- $(\Delta x, \Delta y, \Delta z)$ : projection-center shift.
- $\theta', \sigma', \psi'$ : Euler angles to represent an orthogonal matrix:

$$g(\theta', \sigma', \varphi') = \begin{pmatrix} \cos \theta' & \sin \theta' & 0 \\ -\sin \theta' & \cos \theta' & 0 \\ 0 & 0 & 1 \end{pmatrix} \times \begin{pmatrix} 1 & 0 & 0 \\ 0 & \cos \sigma' & \sin \sigma' \\ 0 & -\sin \sigma' & \cos \sigma' \end{pmatrix} \begin{pmatrix} \cos \varphi' & \sin \varphi' & 0 \\ -\sin \varphi' & \cos \varphi' & 0 \\ 0 & 0 & 1 \end{pmatrix}.$$

- unit-cell parameters represented by the five entries of the lower triangle matrix:

$$A := \begin{pmatrix} 1 & 0 & 0 \\ a_{21} & a_{22} & 0 \\ a_{31} & a_{32} & a_{33} \end{pmatrix}.$$

The above  $A$  is obtained by applying the Cholesky decomposition to the following symmetric matrix, and setting  $a^*$  to 1 in order to normalize the scale:

$$\begin{aligned} AA^T &= \begin{pmatrix} (a^*)^2 & a^*b^* \cos \gamma^* & a^*c^* \cos \beta^* \\ a^*b^* \cos \gamma^* & (b^*)^2 & b^*c^* \cos \alpha^* \\ a^*c^* \cos \beta^* & b^*c^* \cos \alpha^* & (c^*)^2 \end{pmatrix} \\ &= \begin{pmatrix} a^2 & ab \cos \gamma & ac \cos \beta \\ ab \cos \gamma & b^2 & bc \cos \alpha \\ ac \cos \beta & bc \cos \alpha & c^2 \end{pmatrix}^{-1}, \end{aligned} \quad (4)$$



where  $a^*, b^*, c^*, \alpha^*, \beta^*, \gamma^*$  are the reciprocal unit-cell parameters, and  $a, b, c, \alpha, \beta, \gamma$  are the unit-cell parameters.

When a Kikuchi band corresponds to the Miller index  $m(hk\ell)$ , the foot  $(X^{cal}, Y^{cal})$  of the perpendicular from the pattern center to the Kikuchi band, can be computed by:

$$X^{cal} = \frac{-xz}{x^2 + y^2}(1 - \Delta z) + \Delta x, \quad (5)$$

$$Y^{cal} = \frac{-yz}{x^2 + y^2}(1 - \Delta z) + \Delta y, \quad (6)$$

where  $x, y, z$  are the parameters computed by:

$$\begin{pmatrix} x & y & z \end{pmatrix} \underset{def}{=} m \begin{pmatrix} h & k & \ell \end{pmatrix} Ag(\theta', \sigma', \varphi'). \quad (7)$$

$X^{cal}, Y^{cal}$  are independent of the choice of  $m$ . From Eqs.(5), (6),  $\Delta z$  and the scale of the  $z$ -axis cannot be simultaneously determined only from  $(X^{cal}, Y^{cal})$ . In order to obtain both, it is necessary to use the bandwidths calculated by:

$$\beta^{cal} = (\tan(\sigma^{cal} + \theta^{cal}) - \tan(\sigma^{cal} - \theta^{cal}))(1 - \Delta z). \quad (8)$$

The values of  $\sigma^{cal}$  and the Bragg angle  $\theta^{cal}$  are computed by

$$\begin{aligned} \sigma^{cal} &= \arctan(z/\sqrt{x^2 + y^2}), \\ \theta^{cal} &= \arcsin(s\lambda\sqrt{x^2 + y^2 + z^2}/2), \end{aligned}$$

where  $s$  is the scale of the unit cell (required by the above scaling of  $A$ ), and  $\lambda$  is the wavelength of the electron beam. Although the uncertainty in the value of  $\lambda$  has been pointed out [Nolze and Winkelmann, 2017], it can be included in the uncertainty in band widths. Therefore,  $\lambda$  is fixed to the input value.

The refinement process is carried out by non-linear least squares method of the Levenberg-Marquardt algorithm. The parameters obtained in the indexing process are used as the initial parameters of  $s$  and  $A$ . The integers  $m$  in Eq.(7) are reassigned in every iteration of the refinement process, by checking which  $m$  gives the  $\beta^{cal}$  closest to the observed  $\beta^{obs}$ .

## 4 De Wolff figures of merit for EBSD indexing

Some sorting system is required for finding the most plausible one from the multiple candidate solutions in a short time. For the orientation determination of the EBSD patterns, the *Confidence Index* (CI, Field (1997)) based on the number of “votes” (Wright(1992), the *Fit* based on the difference between the computed bands and the detected bands), and the *Image Quality* (IQ) are used.

Herein, use of the idea of the de Wolff figure of merit  $M_n$  is proposed. Although a number of new figures of merit have been proposed for powder indexing,  $M_n$  has been the most efficient indicator in use for long. In particular, it is possible to judge whether or not a plausible solution is included in the output, just by checking the largest value of  $M_n$ . In Section 5, we shall see that its generalizations to 2D and 3D data also have this property.

The de Wolff figure of merit  $M_n$  evaluates the similarity between the set of observed  $q$ -values ( $= 1/d^2$ ,  $d$ :  $d$ -spacing)  $0 < Q_1^{obs} < \dots < Q_n^{obs}$  and the set of computed  $0 < q_1 < \dots < q_N$  by:

$$M_n = \bar{\epsilon}/\delta, \quad (9)$$

where  $\bar{\epsilon}$  and  $\delta$  are the *average discrepancy* and the *actual discrepancy*, respectively, which are defined by:

$$\begin{aligned} \bar{\epsilon} &:= Q_n^{obs}/2N, \\ \delta &:= \frac{1}{n} \sum_{i=1}^n |Q_i^{obs} - Q_i^{cal}|, \\ Q_i^{cal} &: \text{computed } q\text{-value closest to the observed } Q_i^{obs}. \end{aligned}$$

When it is assumed that  $Q_i^{obs}$  ( $i = 1, \dots, n-1$ ) and  $q_i$  are uniformly distributed in the interval  $[0, Q_n^{obs}]$ , the  $\bar{\epsilon}$  in Eq.(10) is an approximation of the mean value of  $\delta$  (Wu (1988)). Namely, the expected value of the shortest distance between  $Q$  and  $q_1, \dots, q_n$  equals:

$$\bar{\epsilon} \approx E \left[ \min_{i=1, \dots, N} \{|Q - q_i|\} \right].$$

In Appendix C, this idea is extended to data of general dimensions. In particular, the obtained figures of merit is scale-free, similarly to the original  $M_n$ .

If a set of computed points  $x_1, \dots, x_N$  and  $X$  are uniformly distributed in an  $s$ -dimensional hypersphere of radius  $R$ , the expected value of the shortest distance between  $\{x_1, \dots, x_N\}$  and  $X$  can be approximated by the following asymptotic formula:

$$E \left[ \min_{i=1, \dots, N} \{|X - x_i|\} \right] \sim \frac{\Gamma(1/s)}{s} \frac{R}{N^{1/s}},$$

where  $\Gamma(z)$  is the Gamma function  $\int_0^\infty t^{z-1} e^{-t} dt$ . By using the volume  $V = (\sqrt{\pi}R)^s / (\Gamma(s/2 + 1)N)$  of the  $s$ -dimensional hypersphere, the following is obtained:

$$E \left[ \min_{i=1, \dots, N} \{|X - x_i|\} \right] \sim \frac{\Gamma(s/2 + 1)^{1/s} \Gamma(1/s)}{\sqrt{\pi}s} (V/N)^{1/s}. \quad (10)$$

For any point configuration in a convex body of volume  $V$ , Eq.(10) holds, because the influence of the boundary can be ignored for sufficiently large  $N$ .

In particular, the formulas for the dimensions  $s = 2, 3$  are:

**(Case of 2D objects of volume  $V$ )**

$$E \left[ \min_{i=1, \dots, N} \{|X - x_i|\} \right] \sim \frac{1}{2} (V/N)^{1/2}. \quad (11)$$

**(Case of 3D objects of volume  $V$ )**

$$\begin{aligned} E \left[ \min_{i=1, \dots, N} \{|X - x_i|\} \right] &\sim \Gamma(1/3) \left( \frac{V}{36\pi N} \right)^{1/3} \\ &\approx 2.6789 \left( \frac{V}{36\pi N} \right)^{1/3}. \end{aligned} \quad (12)$$

In the following examples, it is explained how Eqs.(11) and (12) can be used for orientation determination and ab-initio indexing.

**Example 1** (For comparison of band positions)

The feet  $P_i^{obs} = (X_i^{obs}, Y_i^{obs})$  ( $i = 1, \dots, n$ ) of the perpendiculars from the pattern center to the Kikuchi bands, can be regarded as a set of coordinates distributed in a 2D circle of radius  $R := \max_{i=1, \dots, n} \{(X_i^{obs})^2 + (Y_i^{obs})^2\}$ . If  $(X_j^{cal}, Y_j^{cal})$  ( $j = 1, \dots, N$ ) are the computed band positions in the circle, these two sets can be compared by setting  $V$  in Eq.(11) to the area  $V = \pi R^2$  of the circle; the ratio  $M_{n,N} = \bar{\epsilon}/\delta$  is computed by:

$$\begin{aligned} \bar{\epsilon} &:= \frac{R}{2} \sqrt{\frac{\pi}{N}}, \\ \delta &:= \frac{1}{n} \sum_{i=1}^n |P_i^{obs} - P_i^{cal}|, \end{aligned}$$

where  $P_i^{cal} = (X_i^{cal}, Y_i^{cal})$  is the computed point closest to  $P_i^{obs}$ .

**Example 2** (For comparison of band positions and widths)

The 3D coordinates representing the Kikuchi bands are obtained by considering the bandwidths  $\beta_i^{obs}$  as the third coordinates:

- $\mathcal{P}_i^{obs} = (X_i^{obs}, Y_i^{obs}, \beta_i^{obs})$  ( $i = 1, \dots, n$ ),
- $(X_j^{cal}, Y_j^{cal}, \beta_j^{cal})$  ( $j = 1, \dots, N$ ), where  $\beta_j^{cal}$  is approximated by using Eq.(8) and the following:

$$\begin{aligned}\sigma^{cal} &= \arctan(z/\sqrt{x^2 + y^2}), \\ 2\theta^{cal} &\approx 2\sin\theta^{cal} = s\lambda\sqrt{x^2 + y^2 + z^2}.\end{aligned}$$

The above  $\mathcal{P}_i^{obs}$  are distributed in the cylinder with the radius  $R = \max_{i=1, \dots, n} \{(X_i^{obs})^2 + (Y_i^{obs})^2\}$  and the height  $h = \max_{i=1, \dots, n} \{\beta_i^{obs}\}$ . Therefore,  $V$  in Eq.(12) is set to  $\pi R^2 h$ . The figure of merit  $M_{n,N} = \bar{\epsilon}/\delta$  is computed by:

$$\begin{aligned}\bar{\epsilon} &:= \Gamma(1/3) \left( \frac{R^2 h}{36N} \right)^{1/3}, \\ \delta &:= \frac{1}{n} \sum_{i=1}^n |\mathcal{P}_i^{obs} - \mathcal{P}_i^{cal}|.\end{aligned}$$

where  $\mathcal{P}_i^{cal} = (X_i^{cal}, Y_i^{cal}, \beta_i^{cal})$  is the computed point closest to  $\mathcal{P}_i^{obs}$ .

In the definition, the number of computed points  $N$  is also a parameter, because infinitely many non-visible bands are theoretically included in the range of the observed EBSD pattern. This  $N$  can be automatically determined, by setting the upper thresholds for the  $d$ -values and imposing the following constraint on the generated Miller indices.

- for each indexing solution, the upper threshold for the  $d$ -values of the computed bands is set to the minimum value required to assign a Miller index to every observed band.
- In  $(X_i^{cal}, Y_i^{cal})$  ( $i = 1, \dots, N$ ), overlapping bands  $m(hk\ell)$  ( $m \neq 0$ : integer) appear only once. Namely, only the narrowest bandwidths  $\beta_j^{cal}$  are contained and compared.

By doing the above, solutions that can assign  $hk\ell$  with smaller  $|h|, |k|, |\ell|$  to the bands, obtain larger  $M_{n,N}$ . This is a heuristic for ranking the true solution above the derivative lattices. Very flat or thin unit cells, are less likely to be selected consequently.

## 5 Computational results and discussion

The proposed method was implemented using C++, and applied to the analysis of dynamically simulated Kikuchi patterns (Figures 1–4 in Appendix B) and experimental patterns (Figures 7–8). The program was run on an Intel Core i7-5930k CPU (3.50 GHz) without parallel computation. The results are presented in Tables 2 and 3.

The quick search and exhaustive search were carried out by using the algorithm in Table 1. The only difference between them is that the check (\*) in the footnote of Table 1 is performed in the former search. The search parameters commonly used for the test, are listed in Table 1 of Appendix A.

The simulated patterns were created by using the Bruker's commercial software *DynamicS* [Winkelmann et al., 2007]. The parameters used for the simulation are presented in Table 1 of Appendix B. In particular, the used coordinates of the projection centers were exact.

The experimental EBSD patterns were prepared by using an SEM-EBSD system (JEOL 7001F-EDAX DigiView camera) with the 20kV electron-accelerating voltage and the beam current up to 14nA. Hence, the wavelength of the electron beam is  $8.588510^{-12}m$  (relativistic effects are considered). Precise projection centers were also available for these experimental data, since the second author used the pattern matching technique to obtain them (see Nolze *et al.* (2017); this technique requires pattern simulation based on the phase information). Therefore, the results for imprecise projection centers are also presented, after the results for the precise projection centers.

For the test, the band slopes, its perpendiculars and band widths were manually extracted (without checking band profiles), because the existing automatic methods could not obtain satisfactory results.

In order to obtain a reliable indexing result, at least more than a dozen of band coordinates should be prepared. However, software development for extracting many band edges is not the scope of this article. More precisely, visually recognizable dark lines surrounding a bright band were used as the band edges.

In band searching without assuming the band-profile model, it is basically impossible to estimate precise errors of the parameters  $\varphi$ ,  $\sigma$  to represent the band coordinates (Figure 1) and  $\sigma \pm \theta$  to represent the band widths (Eq.(2)). Therefore, all the error values of the input angles are estimated to 1 degree, and used to calculate the propagation errors of the unit cell parameters. The error does not seem to be overestimation, considering the obtained propagation errors (Tables 2–3). In particular, large errors in the band widths are justified by the uncertainty of the wavelength due to the energy loss of the electron, and the ambiguity in the definition of the band width. Comparing to these factors, the influence of the accelerating voltage error is small.

In Figures 7, 8, the yellow lines present the band slopes used to determine the band edges. The band positions are the midpoints of the band edges if the spherical coordinates  $(\sin \sigma \cos \varphi, \sin \sigma \sin \varphi, \cos \sigma)$  are used.

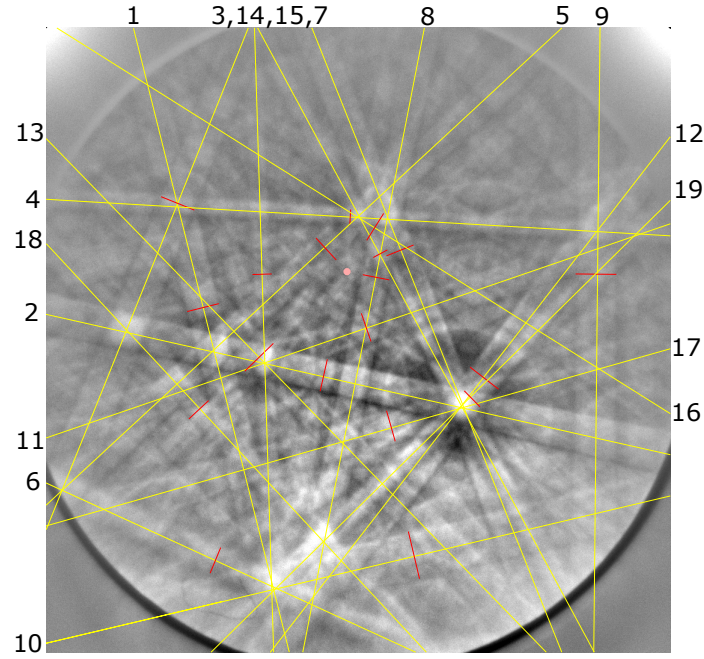


Figure 7: Band slopes and widths extracted from an experimental pattern of Cementite ( $1040 \times 1040 \text{ px}^2$ )

When precise projection centers were used, the program succeeded in acquisition of the correct cell, except for the two triclinic cases among 6 test data. The new figures of merit ranked it at the top among the solutions of the same Bravais type. However, the scales of the obtained unit-cell parameters are 2.1–8.9 % smaller than the literature values.

Owing to the inaccuracy of the used band widths, the  $M_{n,N}$  values in Table 3 are smaller than those in Table 2. In particular, rather small  $M_{n,N} = 4.33$  was obtained for the cementite sample when the bandwidths were used, although the solution was almost identical to the case without band widths.

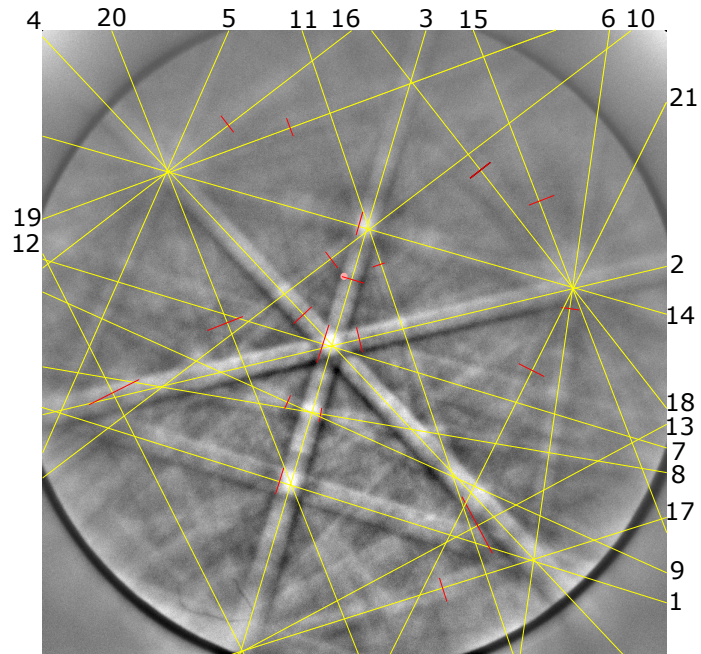


Figure 8: Band slopes and widths extracted from an experimental pattern of Silico Ferrite of  $Ca$  &  $Al$  ( $1040 \times 1040 \text{ px}^2$ )

Table 2: Comparison of the optimal indexing solutions and the parameters in the literature (when bandwidths are not used<sup>a</sup>)

Number of used bands	Success/Failure in quick search (time (sec.), $M_{n,N}$ )	Success/Failure in exhaustive search (time (sec.), $M_{n,N}$ )	$a/c$ (error <sup>b</sup> )	$b/c$ (error <sup>b</sup> )	$\alpha$ (deg.) (error <sup>b</sup> )	$\beta$ (deg.) (error <sup>b</sup> )	$\gamma$ (deg.) (error <sup>b</sup> )
<b>Simulated patterns:</b>							
<b>Ni</b> (cubic(F), $a/c = b/c = 1$ ):							
20	S (7.40, $M_{20,41} = 46.60$ )	S (243.83, $M_{20,41} = 47.56$ )	1	1	90	90	90
<b>Fe</b> (cubic(I), $a/c = b/c = 1$ ):							
23	S (11.78, $M_{23,57} = 57.73$ )	S (426.62, $M_{23,58} = 59.03$ )	1	1	90	90	90
<b>Zn</b> (hexagonal, $a/c = b/c = 0.5387$ ):							
23	S (3.17, $M_{23,107} = 39.47$ )	S (144.68, $M_{23,105} = 39.85$ )	0.540 (0.008)	0.540 (0.008)	90	90	120
<b>Silico-ferrite of calcium and aluminum</b> (triclinic, $a/c = 0.881$ , $b/c = 0.897$ , $\alpha = 94.11$ , $\beta = 111.4$ , $\gamma = 110.3$ ):							
22	F (3.26)	F <sup>c</sup> (339.39, $M_{22,301} = 21.73$ )	0.589 (0.007)	0.588 (0.009)	89.82 (0.78)	106.99 (1.01)	119.95 (0.83)
<b>Experimental patterns:</b>							
<b>Spheroidal cementite</b> (orthorhombic (P), $a/c = 0.6711$ , $b/c = 0.7546$ ):							
19	F (0.91)	S (20.03, $M_{19,271} = 16.73$ )	0.663 (0.011)	0.745 (0.012)	90	90	90
<b>Silico-ferrite of calcium and aluminum</b> (triclinic, $a/c = 0.881$ , $b/c = 0.897$ , $\alpha = 94.11$ , $\beta = 111.4$ , $\gamma = 110.3$ ):							
21	F (0.77)	F <sup>c</sup> (53.67, $M_{21,347} = 7.75$ )	0.764 (0.013)	0.829 (0.017)	91.37 (1.13)	100.36 (1.04)	102.29 (0.76)

<sup>a</sup>The pattern-center shift  $\Delta z$  in the direction perpendicular to the screen was fixed to 0 for low-symmetric cells, considering the ambiguity pointed out by Alkorta (2013).

<sup>b</sup>These error values are computed as the propagation errors of the estimated error 1 degree of the input angles  $\sigma$ ,  $\varphi$  and  $\sigma \pm \theta$  (see Figure 1 and Eq.(2)).

<sup>c</sup>These triclinic cases are regarded as failures, since the differences in the length-ratios and angles from the literature values exceeded 10%, although all the bands were indexed. For the simulated pattern, as seen from  $3a : 3b : 2c = 0.884 : 0.881 : 1$ , the parameters that attained the largest  $M_{n,N}$  value among triclinic solutions, are close to those of the derivative lattice of the true solution.

Table 3: Comparison of the optimal indexing solutions and the parameters in the literature when bandwidths are used

Number of used bands	Success/Failure in quick search (time (sec.), $M_{n,N}$ )	Success/Failure in exhaustive search (time (sec.), $M_{n,N}$ )	$a(\text{\AA})$ (error <sup>b</sup> )	$b(\text{\AA})$ (error <sup>b</sup> )	$c(\text{\AA})$ (error <sup>b</sup> )	$\alpha(\text{deg.})$	$\beta(\text{deg.})$	$\gamma(\text{deg.})$
<b>Simulated patterns:</b>								
<b>Ni</b> (cubic(F), $a = b = c = 3.516(\text{\AA})$ ):								
20	S (6.15, $M_{20,41} = 22.62$ )	S (243.13, $M_{20,39} = 23.00$ )	3.397 (0.235)	3.397 (0.235)	3.397 (0.235)	90	90	90
<b>Fe</b> (cubic(I), $a = b = c = 2.866(\text{\AA})$ ):								
23	S (13.82, $M_{23,57} = 37.78$ )	S (426.15, $M_{23,57} = 38.13$ )	2.805 (0.184)	2.805 (0.184)	2.805 (0.184)	90	90	90
<b>Zn</b> (hexagonal, $a = b = 2.665$ , $c = 4.947(\text{\AA})$ ):								
23	S (2.63, $M_{23,103} = 24.29$ )	S (144.41, $M_{23,103} = 24.29$ )	2.567 (0.179)	2.567 (0.179)	4.706 (0.344)	90	90	120
<b>Silico-ferrite of calcium and aluminum</b>								
(triclinic, $a = 10.40$ , $b = 10.59$ , $c = 11.81(\text{\AA})$ , $\alpha = 94.11$ , $\beta = 111.4$ , $\gamma = 110.3(\text{deg.})$ <sup>§</sup> :								
22	F (2.27)	F <sup>c</sup> (289.03)						
<b>Experimental patterns:</b>								
<b>Spheroidal cementite</b> (orthorhombic (P), $a = 4.526$ , $b = 5.089$ , $c = 6.744(\text{\AA})$ [Gardin, 1962]):								
19	F (0.25)	S (20.14, $M_{19,262} = 4.33$ )	4.122 (0.330)	4.659 (0.4121)	6.245 (0.5411)	90	90	90
<b>Silico-ferrite of calcium and aluminum</b>								
(triclinic, $a = 10.40$ , $b = 10.59$ , $c = 11.81(\text{\AA})$ , $\alpha = 94.11$ , $\beta = 111.4$ , $\gamma = 110.3(\text{deg.})$ <sup>d</sup> :								
21	F (1.01)	F <sup>c</sup> (48.49)						

<sup>b</sup>See the footnote of Table 2.

<sup>c</sup>For these triclinic cases, none of the obtained solutions was close to the true solution. However, for the simulated pattern, a triclinic solution attained  $M_{22,167} = 8.82$  and all the input bands were indexed.

<sup>d</sup>The unit-cell parameters were obtained by the Rietveld refinement of X-ray diffraction data (a little distinct from the literature values in Takayama *et. al.* (2018), owing to the different composition)

Table 4: Influence of the projection center shift ( $\Delta x, \Delta y, \Delta z$ ), when bandwidths are not used; results for the 343 cases given by  $\Delta x/z, \Delta y/z, \Delta z/z = 0, \pm 0.005, \pm 0.01$  or  $\pm 0.02$  ( $z$ : camera length)

Used search method	Number of failed cases (+ number of failed cases in Bravais lattice determination)	Range of obtained solutions				
		$a/c$	$b/c$	$\alpha(\text{deg.})$	$\beta(\text{deg.})$	$\gamma(\text{deg.})$
<b>Ni</b> (simulated, cubic(F), $a/c = b/c = 1$ ):						
Quick search	0 (+0) / 343	1	1	90	90	90
<b>Fe</b> (simulated, cubic(I), $a/c = b/c = 1$ ):						
Quick search	0 (+1) / 343	1	1	90–90.47		
<b>Zn</b> (simulated, hexagonal, $a/c = b/c = 0.5387$ ):						
Quick search	0 (+0) / 343	0.526–0.555		90	90	120
<b>Spheroidal cementite</b> (experimental, orthorhombic (P), $a/c = 0.6711$ , $b/c = 0.7546$ ):						
Exhaustive search	0 (+0) / 343	0.643–0.684	0.734–0.757	90	90	90
						8.64–21.22



Table 5: Influence of the projection center shift ( $\Delta x, \Delta y, \Delta z$ ), when bandwidths are used; results for the 343 cases given by  $\Delta x/z, \Delta y/z, \Delta z/z = 0, \pm 0.005, \pm 0.01$  or  $\pm 0.02$  ( $z$ : camera length).

Used search method	Number of failed cases (+ number of failed cases in Bravais lattice determination)	Range of obtained solutions					$M_{n,N}$
		$a$ (Å)	$b$ (Å)	$c$ (Å)	$\alpha$ (deg.)	$\beta$ (deg.)	$\gamma$ (deg.)
<b>Ni</b> (simulated, cubic(F), $a = b = c = 3.516(\text{Å})$ ): Quick search	0 (+0) / 343		3.228–3.535		90	90	14.94–23.69
<b>Fe</b> (simulated, cubic(I), $a = b = c = 2.866(\text{Å})$ ): Quick search	0 (+0) / 343		2.724–2.962		90	90	4.63–38.09
<b>Zn</b> (simulated, hexagonal, $a = b = 2.665, c = 4.947(\text{Å})$ ): Quick search	0 (+28) / 343	2.405–2.718		4.468–5.051	87.88–92.51	118.62–120	11.27–27.48
<b>Spheroidal cementite</b> (experimental, orthorhombic (P), $a = 4.526, b = 5.089, c = 6.744(\text{Å})$ ; Gardin (1962)): Exhaustive search	5 (+15) / 343	3.86–4.36	4.29–4.90	5.74–6.60	90	89.22–93.04	3.32–4.50

For each sample with the exception of the failed triclinic case, we prepared  $7^3 = 343$  different sets of band coordinates, by perturbing the projection center. The shifts used to make the input  $\varphi, \sigma$  are as follows:

$$\frac{\Delta x}{z}, \frac{\Delta y}{z}, \frac{\Delta z}{z} = 0, \pm 0.005, \pm 0.01, \pm 0.02. \quad (z: \text{camera length})$$

Our software stably obtained the correct solutions for any cases in which  $\sqrt{(\Delta x/z)^2 + (\Delta y/z)^2 + (\Delta z/z)^2} \leq 0.02$ . The results are presented in Tables 4, 5. The presented unit-cell parameters have been refined by the least-squares method. If a unit cell close to the correct one obtains the largest  $M_{n,N}$  value among the unit cells in the same Bravais type, it is counted as a success. In order to see the influence of imprecise projection centers on the indexing solutions, the  $M_{n,N}$  values in (i) the cementite case when bandwidths are not used, and (ii) the  $Fe$  case when bandwidths are used, are presented in Figure 9.

When the number of bands used in ab-initio indexing was reduced by half, no correct answer was obtained for the  $Zn$  and Cementite samples, even by the exhaustive search. In particular, for the  $Zn$  sample, a low-symmetric derivative lattice of the hexagonal lattice was output. Since all the bands were indexed by the derivative lattice, the  $M_{n,N}$  value was still more than 20.

This indicates that the ambiguity problem is more likely to happen, if a smaller number of bands are used. The  $M_{n,N}$  values when the indexing was successful for a smaller number of bands, are presented in (iii), (iv) of Figure 9. As also deduced from the definition, the  $M_{n,N}$  tends to be larger, when the number of bands to fit is small.

## 6 Discussion

It is known that the de Wolff  $M_n$  attains a large value (*e.g.*,  $> 10$ ) for very plausible solutions, and does not exceed 3 for invalid solutions [de Wolff, 1968]. The following are the other well-known properties of the de Wolff  $M_n$ :

- (a)  $M_n$  is sensitive to the existence of reflections observed but not computed from the model, and insensitive to the reflections computed but not observed in the pattern, because of the asymmetric definition of  $M_n$  with regard to the observed and calculated reflection sets.
- (b) The value of  $M_n$  generally decrease as  $n$  increases more than 20, because more unprecise  $d$ -values are used as a result.
- (c) If two unit cells with almost identical parameters but distinct Bravais types are compared, the higher-symmetric cell attains a larger  $M_n$ , because the peak overlap caused by the symmetry make the number of computed reflections smaller.

According to its definition,  $M_{n,N}$  also has the property (a), which is desirable for use in EBSD indexing, because there are a number of computed but not observed bands in EBSD patterns. As for (b),  $M_{n,N}$  also reflects the accuracy of observation, similarly to the other statistical criteria, such as chi-square values.

Although it is possible to change the definition of  $M_{n,N}$  so that it has the property (c), this was not adopted, so the current  $M_{n,N}$  does not possess the property (c), as seen from the values in Table 6, because band overlapping occurs regardless of the symmetry.

However, even if the current  $M_{n,N}$  is used, plausible solutions with the highest-symmetry can be easily found, just by checking the output list as in Table 6. As seen from Table 6, the figures of merit also work well to judge which Bravais type is the true. For example, in the case of  $Ni$ , the  $M_{n,N}$  values of the cubic (P, I) solutions were much smaller than those provided to the cubic(F) solutions. The same thing is observed, when the cubic(P, F) and cubic(I) solutions for the  $Fe$  pattern, and the hexagonal and trigonal solutions for the  $Ni$  pattern are compared. Considering that all the derivative lattices can index the same band positions and widths, this is probably owing to our heuristics used when computed reflections are generated, which was described in the last two paragraphs of Section 4.

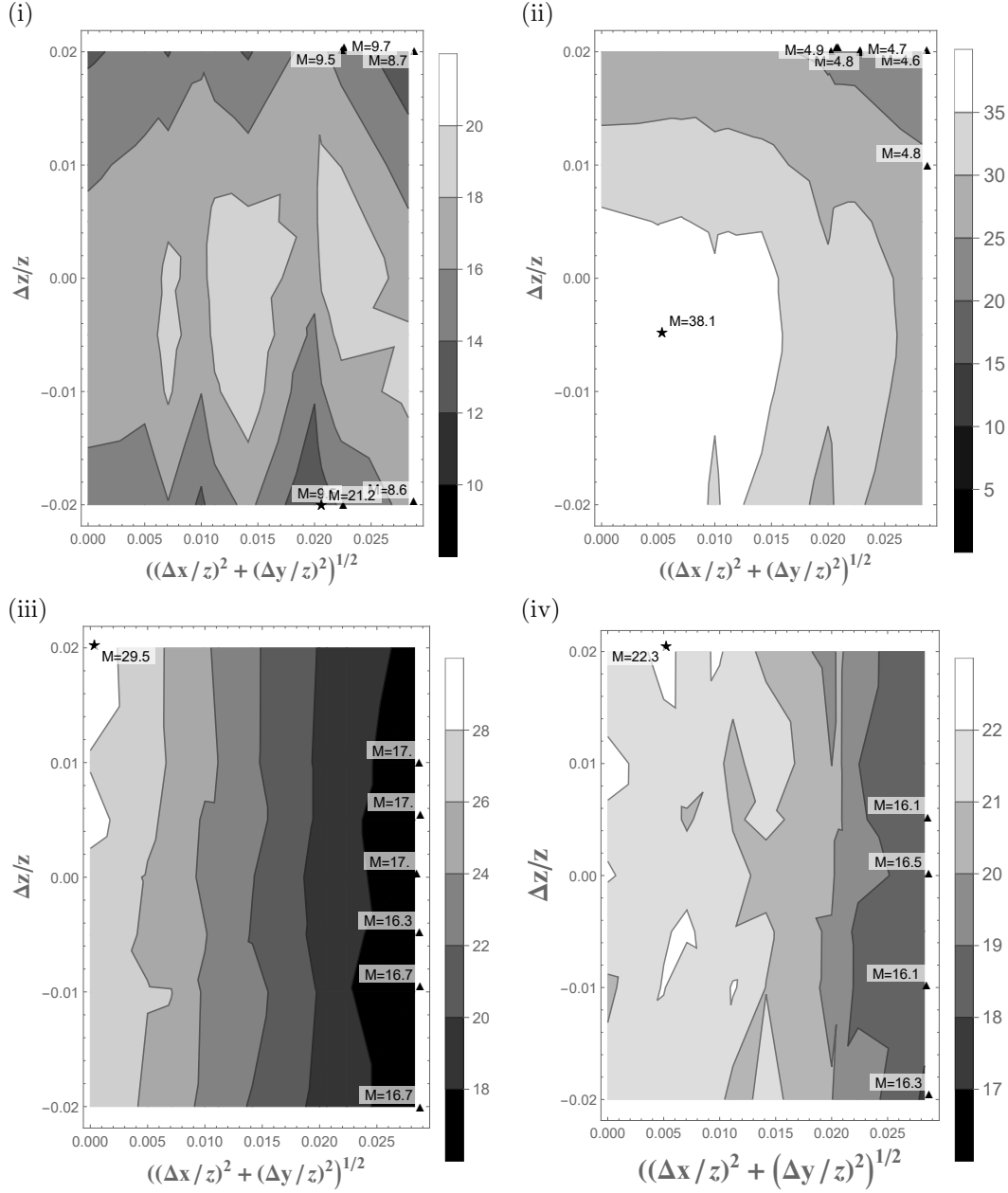


Figure 9: Values of the figures of merit of the optimal indexing solutions in (i) cementite case for 19 bands (bandwidths were not used), (ii) *Fe* case for 23 bands (bandwidths were used), (iii) *Fe* case for 11 bands (bandwidths were used), (iv) *Ni* case for 10 bands (bandwidths were used); the contours represent the interpolation of the largest  $M_{n,N}$  values obtained for the various shifts described in Tables 4–5. The ▲ marks indicate the shifts  $(\Delta x, \Delta y, \Delta z)$  for which the  $M_{n,N}$  values were rather small. The shifts for which  $M_{n,N}$  took the maximum value, are also presented with ★ for reference. The  $M_{n,N}$  value can be large even if the initial shift is large, since unit-cell parameters and the projection center are refined after indexing.

Table 6: The maximum  $M_{n,N}$  values of each Bravais type (attained in the exhaustive searches in Table 3)

Bravais type	Ni (cubic (F))		Fe (cubic (I))		Zn (hexagonal)		Cementite (orthorhombic (P))	
	Not used	Used	Not used	Used	Not used	Used	Not used	Used
Triclinic	51.54 <sup>a</sup>	23.61	54.36	34.58	42.93	23.95	20.75 <sup>b</sup>	4.33
Monoclinic(P)	< 36	< 12	< 44	< 15	39.70	24.00	20.10 <sup>b</sup>	4.33
Monoclinic(C)	53.90 <sup>a</sup>	23.27	57.35	37.31	42.49	24.47	< 10	< 3
Orthorhombic(P)	< 36	< 12	< 44	< 15	< 30	< 12	16.73 <sup>b</sup>	4.33
Orthorhombic(C)	< 36	< 12	< 44	< 15	40.08	24.14	< 10	< 3
Orthorhombic(I)	53.01 <sup>a</sup>	23.26	52.03	33.99	< 30	< 3	< 10	< 3
Orthorhombic(F)	50.63 <sup>a</sup>	22.96	57.15	36.74	< 3	< 3	< 3	< 3
Tetragonal(P)	< 36	< 12	< 44	< 15	< 30	< 12	< 3	< 3
Tetragonal(I)	52.33 <sup>a</sup>	23.38	54.55	37.85	< 30	< 3	< 3	< 3
Trigonal	46.31 <sup>a</sup>	22.81	59.14	37.96	< 30	< 12	< 3	< 3
Hexagonal	< 3	< 3	< 44	< 15	39.85	24.29	< 3	< 3
Cubic(P)	< 36	< 12	< 44	< 15	< 3	< 3	< 3	< 3
Cubic(I)	< 3	< 3	59.03	38.13	< 3	< 3	< 3	< 3
Cubic(F)	47.56	23.00	< 44	< 3	< 3	< 3	< 3	< 3

Table 7: Indexing result for the cementite pattern; the observed/calculated band positions  $(X, Y)$  and bandwidths  $\beta$  are compared (the following values have no unit, since the camera lengths is set to 1).

Miller index			$(X^{cal}, Y^{cal})$		$(X^{obs}, Y^{obs})$		distance between $(X^{cal}, Y^{cal})$ and $(X^{obs}, Y^{obs})$	$\beta^{cal}$	$\beta^{obs}$
-2	-3	3	-0.3951	-0.0993	-0.3948	-0.0985	0.0008	0.0937	0.0892
<sup>†</sup> 0	0	6	-0.0655	-0.2868	-0.0649	-0.2885	0.0017	0.0893	0.0897
-3	-3	0	-0.4663	0.1836	-0.4653	0.1876	0.0042	0.1041	0.0984
-1	0	-3	0.0090	0.1526	0.0088	0.1499	0.0027	0.0470	0.0401
-2	-3	-3	-0.0600	0.0654	-0.0615	0.0665	0.0019	0.0808	0.0823
-1	0	3	-0.3670	-0.7893	-0.3626	-0.7930	0.0058	0.0813	0.0757
0	4	-3	0.1443	0.0584	0.1477	0.0591	0.0034	0.0861	0.0800
1	4	0	0.0775	-0.0141	0.0790	-0.0154	0.0021	0.0767	0.0739
-1	4	0	0.6853	-0.0091	0.6879	-0.0069	0.0034	0.1126	0.1118
-1	2	5	0.1794	-0.7803	0.1845	-0.7818	0.0053	0.1328	0.1331
1	2	5	0.0536	-0.1553	0.0532	-0.1549	0.0006	0.0826	0.0816
0	4	3	0.3773	-0.2902	0.3747	-0.2907	0.0026	0.1035	0.0990
-1	-2	5	-0.2421	-0.2327	-0.2415	-0.2352	0.0026	0.0896	0.1095
-1	-2	1	-0.2346	-0.0082	-0.2334	-0.0072	0.0016	0.0467	0.0526
<sup>‡</sup> 0	2	-2	0.0870	0.0486	0.0894	0.0482	0.0025	0.0462	0.0440
-1	2	-5	0.0770	0.1222	0.0758	0.1206	0.0020	0.0820	0.0872
0	2	5	0.1253	-0.4276	0.1219	-0.4292	0.0038	0.0933	0.0874
-1	-1	3	-0.4078	-0.3758	-0.4045	-0.3765	0.0033	0.0649	0.0741
<sup>‡</sup> 0	2	2	0.3381	-0.3489	0.3388	-0.3445	0.0045	0.0567	0.0617

<sup>b</sup>From the reflection rules of  $P b n m$  (No.62),  $\{00\ell\}$  ( $\ell$ : odd) may be excluded.

<sup>c</sup> $\{01\bar{1}\}$  and  $\{011\}$  were forbidden by the reflection rules ( $0kl$  with an odd  $k$ ) of  $P b n m$  (No.62).

Table 7 is the indexing result for the Cementite sample. The bandwidths assigned the Miller indices  $(02\bar{2})$  and  $(022)$  were probably due to SA, considering that  $(01\bar{1})$  and  $(011)$  are forbidden by the rules ( $0kl$  with an odd  $k$ ) of  $P b n m$  (No.62). However, influence of non-visible narrowest band widths (and also underestimation of the unit-cell scale) is also observed from the assigned Miller indices (*e.g.*,  $(006)$  and  $(\bar{3}30)$ ).

With regard to the ambiguity pointed out for the first time in this article, when bandwidths are used, it is mainly caused by sublattices  $M$  of the true crystal lattice  $L$  with a small index  $[L : M]$ , because  $M$  can index all the edges of the narrowest bands of  $L$ . However, if the HOLZ rings are used, ambiguity is mainly caused by superlattices  $M$  of  $L$  with small  $[M : L]$ , because the radius of a HOLZ ring is an integer multiple of the shortest length of lattice vectors perpendicular to the corresponding zone [Michael and Eades, 2000]. This indicates that the entire information contained in an EBSD pattern might be able to resolve the ambiguity.

## 7 Conclusion

For ab-initio indexing, a new method based on distribution rules of systematic absence and error-stable Bravais lattice determination was proposed. In addition, the de Wolff figures of merit for 1D powder diffraction patterns were redefined for data of multiple dimension and used in orientation determination and ab-initio indexing. The new figures of merit have properties similar to those of the original de Wolff  $M_n$ , except for the preference for higher-symmetric cells, although it is possible to change the definition of  $M_n$  so that it has such a preference. Even if the current figures of merit are used, users can efficiently find the optimal solution and Bravais type. It was also explained how erroneous band widths can cause ambiguity of solutions, in particular in case of low-symmetric cells.

**Acknowledgments** This study was financially supported by the PREST (JPMJPR14E6). We would like to extend our gratitude to Dr. A. Esmaeili, Ms. T. Ueno of Yamagata University and Mr. S. E. Graiff-

Zurita of Kyushu University, who helped us in coding the software, preparing the input files, and performing the computation.

## References

- [Alkorta, 2013] Alkorta, J. (2013). Limits of simulation based high resolution ebsd. *Ultramicroscopy*, 131:33–38.
- [Day, 2008] Day, A. P. (2008). Spherical ebsd. *Journal of Microscopy*, 230:472–486.
- [de Wolff, 1968] de Wolff, P. M. (1968). A simplified criterion for the reliability of a powder pattern indexing. *J. Appl. Cryst.*, 1:108–113.
- [Dingley and Baba-Kishi, 1986] Dingley, D. J. and Baba-Kishi, K. (1986). *Scanning Electron Microscopy*, 2:383–391.
- [Dingley and Wright, 2009] Dingley, D. J. and Wright, S. I. (2009). Determination of crystal phase from an electron backscatter diffraction pattern. *J. Appl. Cryst.*, 42:234–241.
- [Field, 1997] Field, D. P. (1997). Recent advances in the application of orientation imaging. *Ultramicroscopy*, 67:1–9.
- [Gardin, 1962] Gardin, A. I. (1962). An electron-diffraction study of the structure of cementite. *Soviet Physics-Crystallography (Kristallografiya)*, 7:694–700.
- [Grosse-Kunstleve et al., 2004] Grosse-Kunstleve, R. W., Sauter, N. K., and Adams, P. D. (2004). Numerically stable algorithms for the computation of reduced unit cells. *Acta Cryst.*, A60:1–6.
- [Hahn, 2005] Hahn, T. (2005). *International Tables for Crystallography*, volume A. Springer, fifth edition edition.
- [Kogure, 2003] Kogure, T. (2003). Computer program for beginners to assist interpretation of electron diffraction patterns (japanese). *Short Review & Scientific Communication*, 32:96–101.
- [Langer and Däbritz, 2007] Langer, E. and Däbritz, S. (2007). Investigation of holz rings in ebsd patterns. *Physica Status Solidi (c)*, 6:1867–1872.
- [Li and Han, 2015] Li, L. and Han, M. (2015). Determining the bravais lattice using a single electron backscatter diffraction pattern. *J. Appl. Cryst.*, 48:107–115.
- [Li et al., 2014] Li, L., Ouyang, S., Yang, Y., and Han, M. (2014). Ebsd: a computer program for determining an unknown bravais lattice using a single electron backscatter diffraction pattern. *J. Appl. Cryst.*, 47:1466–1468.
- [Marthinsen and Høier, 1988] Marthinsen, K. and Høier, R. (1988). On the breakdown of friedel’s law in electron backscattering channelling patterns. *Acta Cryst.*, A44:700–707.
- [Michael, 2000] Michael, R. (2000). *Electron Backscatter Diffraction in Materials Science*. New York: Kluwer Academic/Plenum Publishers.
- [Michael and Eades, 2000] Michael, R. and Eades, J. A. (2000). Use of reciprocal lattice layer spacing in electron backscatter diffraction pattern analysis. *Ultramicroscopy*, 81:67–81.
- [Nolze et al., 2015] Nolze, G., Grosse, C., and Winkelmann, A. (2015). Kikuchi pattern analysis of noncentrosymmetric crystals. *J. Appl. Cryst.*, 48:1405–1419.
- [Nolze et al., 2017] Nolze, G., Hielscher, R., and Winkelmann, A. (2017). Electron backscatter diffraction beyond the mainstream. *Crystal Research & Technology*, 52:1600252.
- [Nolze and Winkelmann, 2017] Nolze, G. and Winkelmann, A. (2017). Crystallometric and projective properties of kikuchi diffraction patterns. *J. Appl. Cryst.*, 50:102–119.

- [Oishi-Tomiyasu, 2012] Oishi-Tomiyasu, R. (2012). Rapid bravais-lattice determination algorithm for lattice parameters containing large observation errors. *Acta Cryst.*, A68:525–535.
- [Oishi-Tomiyasu, 2013] Oishi-Tomiyasu, R. (2013). Distribution rules of systematic absences on the conway topograph and their application to powder auto-indexing. *Acta Cryst.*, A69:603–610.
- [Oishi-Tomiyasu, 2016] Oishi-Tomiyasu, R. (2016). A table of geometrical ambiguities in powder indexing obtained by exhaustive search. *Acta Cryst.*, A72:73–80.
- [Takayama et al., 2018] Takayama, T., Murao, R., and M., K. (2018). Quantitative analysis of mineral phases in iron-ore sinter by the rietveld method of x-ray diffraction patterns. *ISIJ Int.*, 58:1069–1078.
- [Tanaka and Wilkinson, 2019] Tanaka, T. and Wilkinson, A. J. (2019). Pattern matching analysis of electron backscatter diffraction patterns for pattern centre, crystal orientation and absolute elastic strain determination. *Ultramicroscopy*, 202:87–99.
- [Troost et al., 1993] Troost, K. Z., Sluis, P., and Gravesteijn, D. J. (1993). Microscale elastic strain determination by backscatter kikuchi diffraction in the scanning electron microscope. *Appl. Phys. Lett.*, 62:1110–1112.
- [Venables and Harland, 1973] Venables, J. A. and Harland, C. J. (1973). *Phil. Mag.*, 27:1193–1200.
- [Wilkinson et al., 2006] Wilkinson, A. J., Meaden, G., and Dingley, D. J. (2006). High-resolution elastic strain measurement from electron backscatter diffraction patterns: New levels of sensitivity. *Ultramicroscopy*, 106:307–313.
- [Winkelmann et al., 2007] Winkelmann, A., Trager-Cowan, C., Sweeney, F., Day, A. P., and P., P. (2007). Many-beam dynamical simulation of electron backscatter diffraction patterns. *Ultramicroscopy*, 107:414–421.
- [Wright and Adams, 1992] Wright, S. I. and Adams, B. L. (1992). Automatic analysis of electron backscatter diffraction patterns. *Metallurgical and Materials Transactions A*, 23:759–767.
- [Wu, 1988] Wu, E. (1988). A modification of the de wolff figure of merit for reliability of powder pattern indexing. *J. Appl. Cryst.*, 21:530–535.